

# DROPLET IMPACT ON LOW TEMPERATURES POROUS STRUCTURE: HEAT TRANSFER CHARACTERIZATION

*Jinjuan Sun\**, *Peiyuan Sun*, *Jianhui Tian*

School of Mechatronic Engineering, Xi'an Technological University, Xi'an, China

*Icing and ice accumulation on blades or cooling apertures in aero-engines along with other mechanical systems present significant hazards to operating efficiency and structural integrity. Porous structures enhance fluid flow and modify thermal conductivity. Therefore, this study examines droplet spreading and heat transfer on subcooled porous surfaces, modelling the interactions between droplets and porous structures based on the multiphase flow-phase field method coupled with a heat transfer module. The model's accuracy and reliability were validated by comparing experimental results with numerical simulations. The dynamics of droplets on porous surfaces are examined in detail, focusing on the influence of Weber number, while emphasizing its effect on the coupled heat transfer during impact on subcooled porous structures. It is found that increasing the Weber number markedly enhances droplet dynamics, resulting in a larger spreading factor and an increased tendency for icing, accompanied by pronounced secondary heat transfer effects, which modify the local heat flux distribution during the impact and solidification processes. When the Weber number increases from 60 to 160, the peak heat flux is observed to increase by approximately 90%. In addition, the reduction in surface wettability leads to distinct penetration and heat transfer modes of the droplet. Specifically, the peak heat flux is lowered by roughly 3% compared with the normal wettability conditions, and no pronounced secondary heat transfer behavior is observed. These results provide theoretical insights into droplet icing behavior and support the development of more effective anti-icing strategies.*

*Keywords* : *droplet impact, icing, heat transfer, wettability*

## **1. Introduction**

Ice formation on the walls of cryogenic equipment directly affects its performance and efficiency. Ice buildup on blades or cooling holes also reduces performance and efficiency. For example, in power line transmission equipment, icing substantially impairs its safety, while in wind turbines, ice formation

can lead to a significant drop in operational efficiency. Therefore, investigating this topic can enhance our understanding of the underlying physical mechanisms of ice formation and accretion, and offer theoretical support for droplet impact dynamics on complex surfaces. Shen et al.<sup>[1]</sup> revealed the mechanism of coupled effects of droplet physical property parameters on droplet wall influence behavior and diffusion film behavior. The effect of surface wettability on seawater impingement icing has been studied by many scholars at home and abroad.<sup>[2][3]</sup> An et al.<sup>[4]</sup> employed hollow metal droplets impacting a cold substrate. The spreading of the metal droplet on the cold substrate is controlled by solidification. Shen et al.<sup>[5]</sup> discovered two freezing modes of the droplet and accurately predicted the freezing period of the droplet owing to volume expansion using the proportionality law. Liu et al.<sup>[6]</sup> found that lower wall temperatures reduced the extent of droplet dispersion and suppressed or entirely abolished retraction and oscillation behaviors. As the Weber number climbed, droplet spreading became more intense. Hu et al.<sup>[7]</sup> Employed a linked solidification and melting Volume of Fluid (VOF) model to evaluate the impact of droplet freezing speed under varied temperature circumstances. Yang et al.<sup>[8]</sup> examined the freezing mechanism of droplets contacting a cold cylinder surface. As the Weber number increases or the surface temperature lowers, the freezing rate and the movement speed of the exterior freezing front increase. Shen et al.<sup>[9]</sup> investigated the droplet impact characteristics under aircraft icing conditions, and produced impact characteristics that differ from typical patterns.

The aforementioned research reveals the influencing elements and impact characteristics of droplet impact on complex surfaces from different aspects. However, it rarely explains the heat transmission and underlying mechanics of droplet impact. Therefore, in this work, a multiphase flow phase-field coupled with a heat transfer module is employed to systematically analyze the heat transfer characteristics and spreading dynamics of droplets impacting on low-temperature porous structures

## **2. Numerical simulation models and methods**

### **2.1. Basic construction of physical models**

Using the multiphase flow phase-field method to analyze droplet impact on low-temperature porous structures, fig. 1 shows the optimized 2D model. By drawing a tangential view of the porous structure from the side and setting the porous structure as the inner wall in the fluid phase-field module, key physical parameters are taken from the internal material library of the software and defined through functional expressions. The initial velocity of the droplet is  $V_0$ , the boundary temperature set to 263.15 K, the droplet diameter is 3 mm, the distance from the top of the droplet to the porous wall is 5.5 mm. In the fluid domain, the reference temperature for volume calculations is 293.15 K. The thermal conductivity  $k$  represents the material's ability to conduct heat and varies with temperature to capture the smooth transition between solid and liquid phases during phase change, the latent heat of fusion  $L_f$  of the phase-change material is 333 kJ·kg<sup>-1</sup>, representing the energy absorbed or released during solidification or melting. To describe momentum damping within the mushy zone, a velocity-suppression constant  $q$  of 0.001 is included to limit flow in partially solidified regions, ensuring numerical stability and physically accurate behavior. The dynamic viscosity of the phase-change material  $\eta$  is defined as a temperature-dependent function, indicating the transition from solid-like to liquid-like behavior and accurately representing the material's flow characteristics. The inner wall pore diameter  $d$  is fixed to 0.2 mm, and the boundary condition is designated as no-slip, this setup is stable and compatible with macro-engineering flow. Due to the complexity of the porous structure, the mesh

density along the droplet motion path is refined, while droplet splashing losses are neglected, ensuring the accuracy of the simulation.

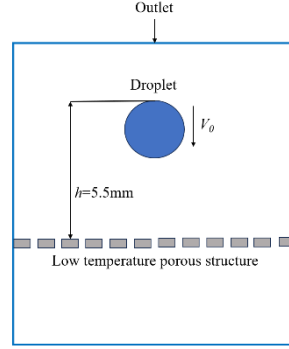


**Figure 1. Optimize the 2D model**

## 2.2. Fluid dynamics methods

The flow field was solved using the VOF method, which is based on the incompressible Navier–Stokes equations:

$$\nabla \cdot (\vec{u}) = 0 \quad (1)$$

$$\frac{\partial(\rho\vec{u})}{\partial t} + \nabla \cdot (\rho\vec{u}\vec{u}) = -\nabla p + \nabla \cdot \mu [(\nabla\vec{u}) + (\nabla\vec{u})^T] + \rho\vec{g} + \overline{F_{ST}} + \vec{S} \quad (2)$$

Where  $\rho$ ,  $\vec{u}$ ,  $p$ ,  $\mu$ , and  $\vec{g}$  indicate density, velocity field, pressure, dynamic viscosity, and gravitational acceleration of the fluid, respectively.

Increasing the contact angle of the porous structure, when a droplet falls freely without starting velocity and strikes the porous structure without penetration, the droplet will bounce upon reaching its maximum spreading radius. According to the droplet impact dynamics formula studied by Reyssat<sup>[10]</sup>:

$$E_k = \frac{2}{3} \pi p R_0^3 V_0^2 \quad (3)$$

$$E_s = \pi r_{\max}^2 \gamma (\cos \theta_r - \cos \theta_d) \quad (4)$$

To account for the impact of the phase transition process on the liquid phase flow, a momentum source term  $S_y$  is introduced. Assuming that the motion in the solid-liquid mixture zone follows Darcy's law, the momentum source term can be represented as:

$$S_y = -\frac{(1-\varphi_{sl})^2}{\varphi_{sl}^3 + \varepsilon} A_{mush} u \quad (5)$$

In the formula,  $\varphi_{sl}$  represents the volume fraction of the liquid phase in the liquid-solid two-phase system;  $A_{mush}$  represents the viscosity coefficient, which is connected to the state of the porous media, and  $\varepsilon$  represents the minimum value.<sup>[11]</sup>

During the process of a droplet contacting a low-temperature wall, a phase transition happens, and water can exist as either a liquid or solid. To precisely characterize the temperature and phase change, based on the research of Brent et al.<sup>[12]</sup>, the liquid fraction  $\beta$ :

$$\beta = \begin{cases} 0 & \text{for } T < T_{\text{solidus}} \\ \frac{T - T_{\text{solidus}}}{T_{\text{liquidus}} - T_{\text{solidus}}} & \text{for } T_{\text{solidus}} < T < T_{\text{liquidus}} \\ 1 & \text{for } T > T_{\text{liquidus}} \end{cases} \quad (6)$$

The formula for computing parameters such as liquid temperature change is as follows:

$$\phi = \phi_w \beta + \phi_i (1 - \beta) \quad (7)$$

Among them,  $\phi$  can be any physical parameter.

### 3. Experimental and numerical simulation validation

#### 3.1. Droplet impact experiment

Figure 2 depicts the experimental setup, which comprises of a droplet generation system, an imaging system, a surface performance measurement system, a droplet impact platform, and a low-temperature refrigeration circulation system. The main equipment of the imaging system is the high-precision high-speed camera (MotionBLITZ EoSens mini2), the data acquisition equipment is primarily (Agilent-34970A), surface performance measurement is completed using Moticom2506, and temperature control in the refrigeration circulation system is achieved using the DC-4015) refrigeration circulation water tank. The experiments were conducted using deionized water droplets, with a density of  $1000 \text{ kg}\cdot\text{m}^{-3}$ , a dynamic viscosity of  $8.937 \times 10^{-4} \text{ Pa}\cdot\text{s}$ , a thermal conductivity of  $0.606 \text{ W}\cdot\text{m}^{-1}\cdot\text{K}^{-1}$ , and a diameter of 3 mm. To ensure the reliability of the validation data, the ambient conditions were strictly controlled in an environmental chamber, where the air temperature was 298.15 K. The porous substrate was made of an alloy with a pore diameter of 0.2 mm, and its temperature was kept constant at 293.15 K, and the droplet release height was adjusted to achieve different impact velocities. High-speed camera was performed at 1000 fps, and the droplet impact data were subsequently processed and integrated using a computer. Each experiment was repeated at least three times to ensure reproducibility and accuracy. All experimental conditions were strictly controlled to guarantee the reliability of the results.

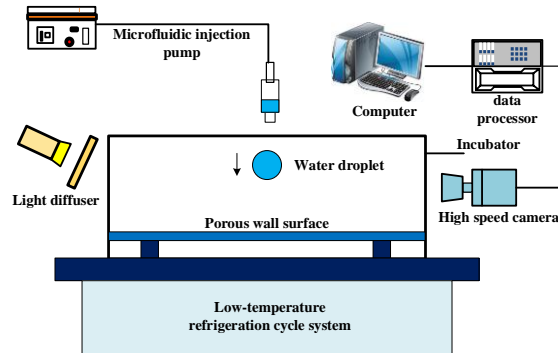
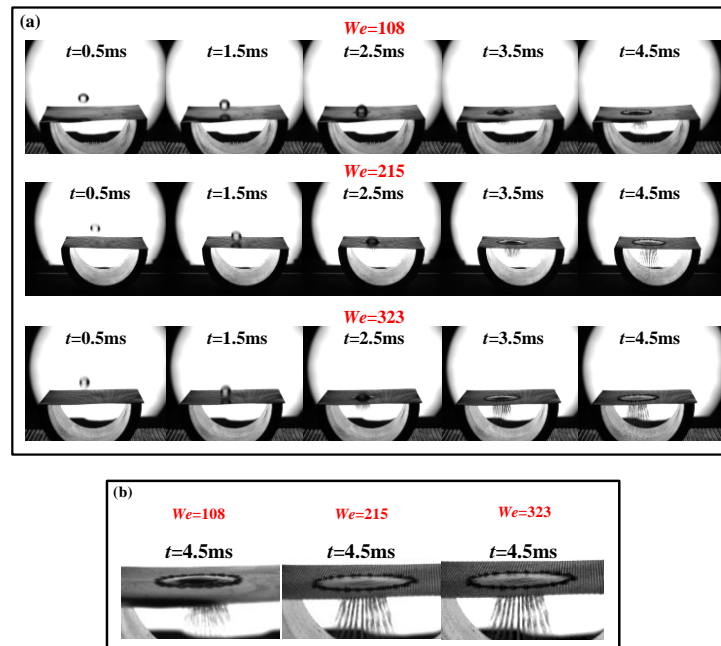


Figure 2. Experimental platform

To validate the accuracy of the physical model, experiments were conducted at initial Weber numbers  $We = 108, 215, \text{ and } 323$ . Fig. 3 (a) presents the droplet impact dynamics under the three conditions, while fig. 3 (b) compares the maximum spreading diameters for  $We = 108, 215, \text{ and } 323$ . It can be observed that the maximum spreading diameters increasing with the Weber number.



**Figure 3. Droplet impact experiment: (a) comparison of impacts at different Weber numbers; (b) comparison of the spread**

### 3.2. Numerical simulation model validation

To perform an in-depth analysis of the impact process, it is required to independently check the accuracy of the physical model. The ratio of the maximum spreading width of the droplet to its original diameter is set as the spreading factor  $n$ . In numerical simulations, the spreading factor is determined by monitoring the maximum border of the droplet spreading. Fig. 4 shows the variation of the droplet spreading factor with mesh size at 4.5 ms for Weber number 108. A coarser mesh underestimates the spreading factor, while the results converge as the maximum mesh cell size decreases below 0.3 mm. Further refinement causes negligible change, ensuring an optimal balance between accuracy and computational cost. At a maximum mesh cell size of 0.1 mm, the spreading factor reaches 3.5, and this mesh size was adopted for all subsequent simulations. Temporal accuracy was ensured by using a fixed time step of 0.1 ms, which is sufficiently small to capture the rapid droplet dynamics and the evolution of the liquid-vapor interface.

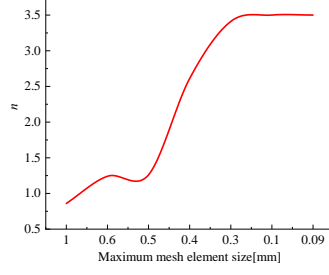


**Figure 4. Mesh independence verification**

Figure 5(a) shows a comparison between experimental and numerical simulations. In the experiment, the droplet was released from a height of 40 cm. To assess experimental reproducibility, each test condition was independently repeated five times. The results presented in this study are based on the averaged value of these five runs. The variations among repeated experiments were small, indicating good reproducibility. Fig. 5(b) shows the curve variations of the spreading factor from experiments and numerical simulations. The numerical results show excellent agreement with the experimental data, with an average deviation of only 0.47%. As seen from the experimental images, the two approaches exhibit a high level of consistency.

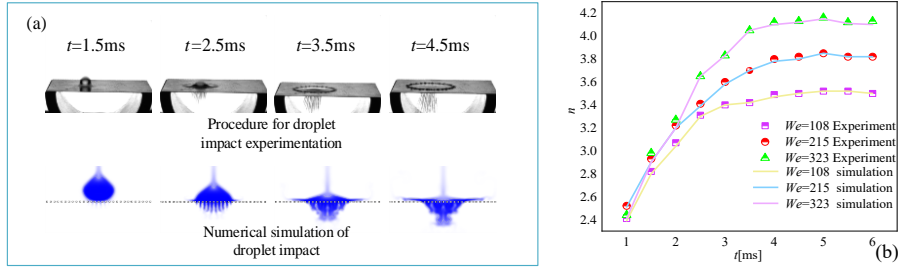


**Figure 5. Comparison of numerical simulation results with experimental results: (a) droplet impact dynamic process; (b) comparison of spreading factor**

## 4. Results and discussion

### 4.1. Permeation mechanism of porous structures

In this study, a larger contact angle corresponds to lower surface wettability, indicating a more hydrophobic behavior of the porous surface. Specifically, the contact angle  $\theta=90^\circ$  is set as the benchmark value for normal wettability. To clarify the influence of the porous structure on permeation behavior, droplets interact with the porous structure at room temperature. The real-time evolution of droplet distribution within the permeation domain is quantified using probe-based measurements, from which the droplet volume change index- $V_1$ .  $V_1$  is introduced as a dimensionless parameter to quantify the temporal evolution of the liquid area within the 2D domain. It is defined as the ratio of the instantaneous liquid area  $A(t)$  to the initial droplet area  $A_0$ :

$$A_0 = \frac{1}{4} \pi D^2 \quad (8)$$

$$V_1 = \frac{A(t)}{A_0} \quad (9)$$

The instantaneous area  $A(t)$  is obtained through numerical integration of the liquid phase volume fraction  $\phi$  over the entire computational domain  $\Omega$ , as defined by:

$$A(t) = \int_{\Omega} \phi dA \quad (10)$$

Figure 6 illustrates the droplet impact dynamics under different wettability conditions. As the Weber number increases, the droplet's vertical kinetic energy is augmented, leading to stronger penetration into the porous substrate. Under the combined effect of inertia and interaction with the substrate, the core region of the droplet exhibits substantial concave deformation, while the spreading width at both ends increases. Conversely, when surface wettability is diminished, the porous structure has a stronger restricting influence on the droplet motion, partially suppressing penetration. These analyses show that droplet spreading and penetration are determined by the combined contributions of droplet inertia and substrate properties. Fig. 7(a) compares the evolution of droplet volume index under different Weber numbers. The results indicate that as the Weber number increases, volume index fluctuations during impact become more pronounced, reflecting a stronger tendency toward penetration. Fig. 7(b) presents the droplet volume index variation curves under different surface wettability. As the surface wettability decreases, the penetration rate gradually falls.

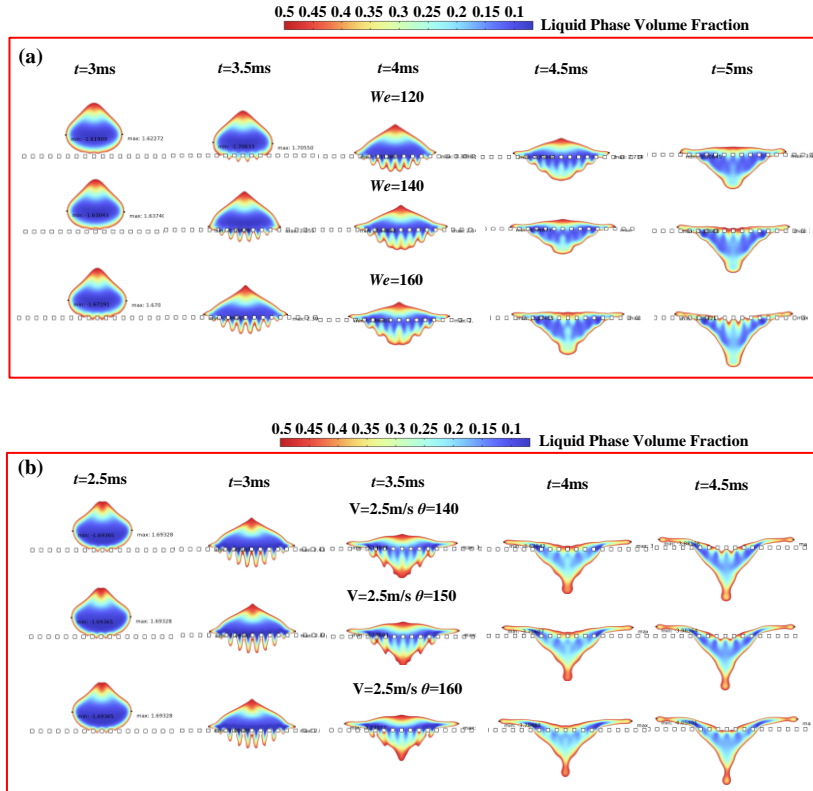
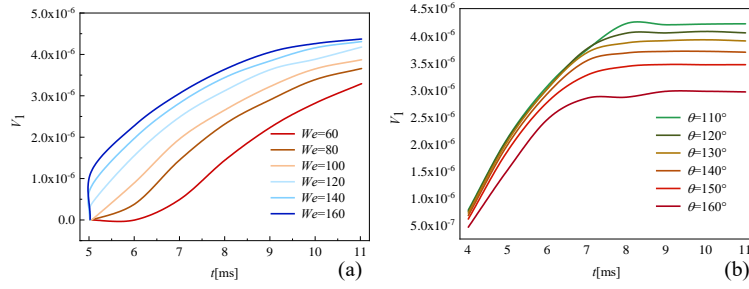


Figure 6. Droplet impact on a porous structure: (a) under different Weber numbers; (b) under different Wettability



**Figure 7. Droplet impact on a room-temperature wall: (a) volume index changes under varying Weber numbers; (b) volume index changes under varied wettability conditions**

## 4.2. Heat transport properties of droplet impact on low-temperature porous materials under varying Weber numbers

### 4.2.1 Analysis of the Impact of Droplet Impact Velocity Distribution and Penetration Process

Figure 8(a) depicts the velocity distribution of droplets at the moment of maximum spreading under different Weber numbers. As the Weber number increases, the tendency for droplet fragmentation becomes more pronounced. At the same time, high-speed regions are mainly concentrated on both sides of the droplet, demonstrating that local flow asymmetry rises with the intensity of the impact. Fig. 8(b) illustrates the velocity vector fields during droplet impact for different Weber numbers. Due to the strong resistance effect of the subcooled surface, the velocity vectors at the droplet periphery generally exhibit an upward deviation. Although the porous structure enhances internal flow within the droplet, the central velocity vectors decrease with increasing Weber number.

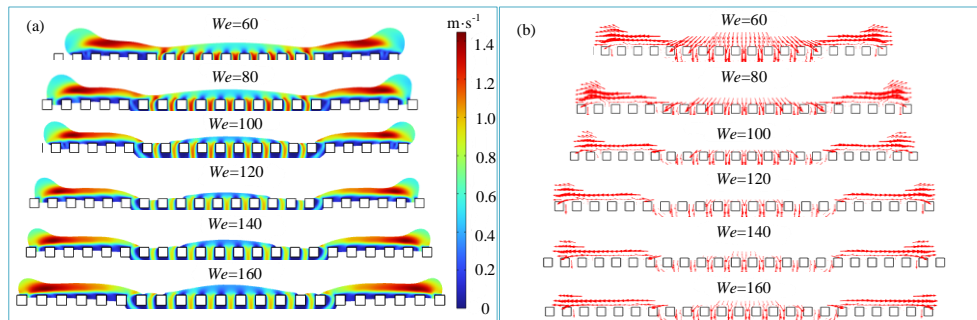


**Figure 8. Cloud map of droplet attaining maximum spreading width: (a) speed distribution map; (b) velocity vector diagram**

Figure 9 illustrates the variation in droplet volume index during impact on a subcooled porous surface under different Weber numbers. Similar to the behavior observed on room-temperature surfaces, the droplet volume index increases with increasing Weber number, indicating enhanced spreading at higher impact intensities. However, under subcooled conditions, the overall magnitude of the volume index is significantly reduced. This reduction is attributed to the occurrence of solidification during impact. At higher Weber numbers, although the droplet spreads more rapidly and covers a larger contact

area, the supercooling conditions promote freezing, leading to an overall suppression of volume evolution compared with room-temperature conditions.

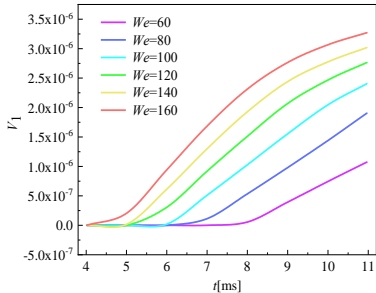


Figure 9. Volume index changes under varying Weber numbers

4.2.2 Heat transfer and thermal evolution between the droplet and the porous structure

As shown in the temperature contour maps in fig. 10, the droplet undergoes immediate heat transfer upon impacting the subcooled porous structure. The cold region gradually propagates into the droplet interior, indicating progressive a continuously enhanced heat transfer process. Moreover, the temperature distribution near the droplet sides becomes increasingly pronounced at later stages. This suggests that local heat transfer becomes more unsteady and intensifies over time. Fig. 11 illustrates the temperature gradient variations. After the droplet impacts the subcooled porous structure, intense heat transfer is primarily concentrated in the contact region between the droplet and the surface. As the droplet continues to spread and penetrate, the intensity of the gradient increases; the temperature gradient extends downward along the droplet penetration direction. A certain degree of lateral spreading is also present, caused by droplet fragmentation during spreading, which affects the horizontal heat transfer.

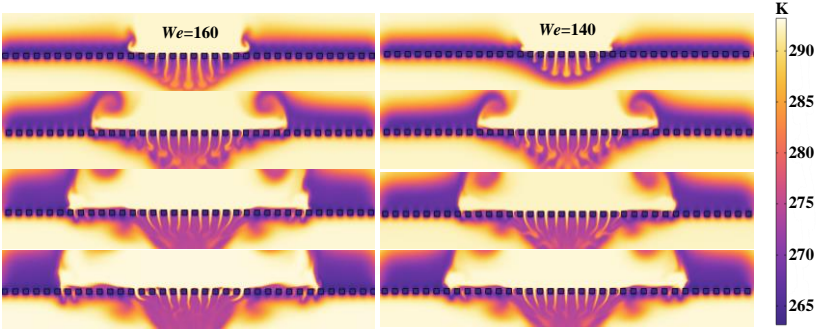


Figure 10. Temperature contour maps under high Weber numbers

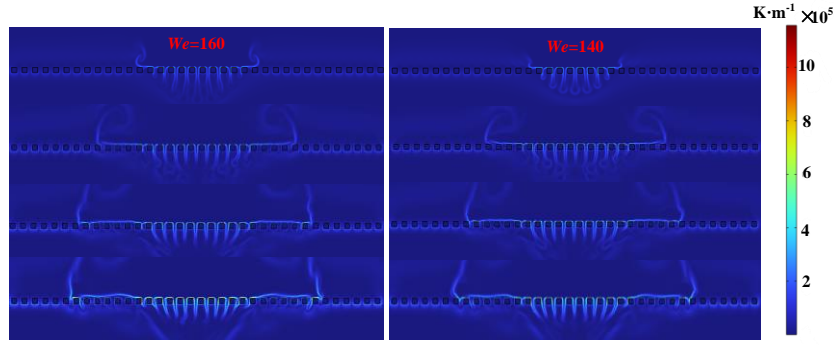


Figure 11. Temperature gradient contour maps under high Weber numbers

The Convective heat flux is shown in fig. 12(a). Detailed analysis reveals that the initial peak corresponds to the early stage of the droplet's contact with the surface, where intense heat transfer causes the heat flux to rise. As the Weber number increases, the peak heat flux also increases. Subsequently, as the droplet spreads and the heat transfer area enlarges, while the temperature difference decreases, the heat flux gradually declines. Influenced by the inertial effect during the initial heat transfer stage and the spreading and penetration behavior, higher Weber numbers correspond to greater droplet impact kinetic energy and spreading, thereby enhancing heat transfer. In the later stage of the curves, a secondary peak is observed at high Weber numbers. The internal phase heat flux on the upper and lower sides is shown in fig. 12(b) and 12(c). Similarly, at high Weber numbers, a secondary heat transfer event occurs during the later stages of droplet impact. As the Weber number increases, droplets are more prone to breakup and splitting during impact. This is accompanied by an increase in spreading width. This fragmentation enhances interfacial disturbances. The smaller size of broken droplets leads to higher heat transfer efficiency, facilitating icing after impact and thereby influencing the overall freezing behavior.

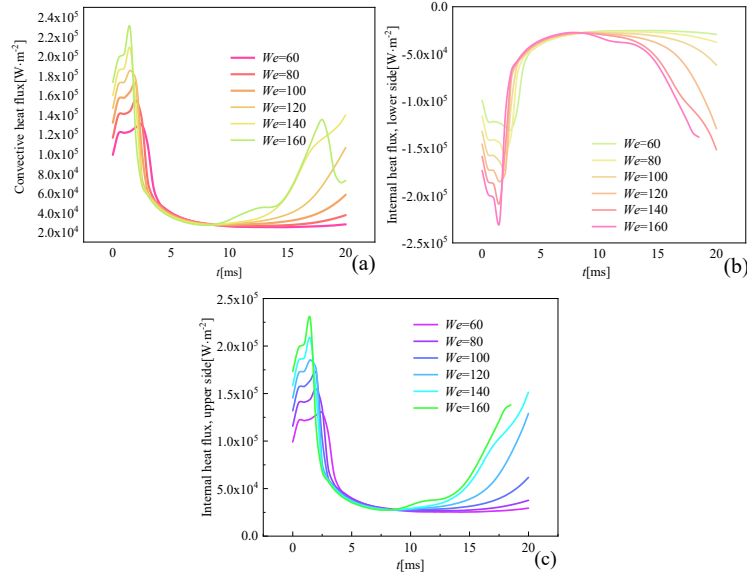


Figure 12. Droplet phase change and heat flux curves: (a) internal convective heat flux curves of the droplet; (b) lower side heat flux curves at the droplet–substrate interface; (c) upper side heat flux curves at the droplet–substrate interface

### 4.3. Coupled Effects of Low-Wettability Porous Structures on Droplet Impact Dynamics and Heat Transfer

#### 4.3.1 Analysis of droplet velocity distribution and penetration process under low wettability conditions

Contact angles in the range of  $100^\circ$  to  $130^\circ$  are highly representative of common hydrophobic coatings used in engineering applications. Consequently, in this subsection, a subcooled porous surface with a contact angle of  $\theta=120^\circ$  was employed to investigate the dynamic characteristics of droplet impact under varying Weber numbers. Fig. 13 presents the velocity magnitude and vector distributions of droplets at the moment of maximum spreading upon impacting a low-wettability porous surface. Under the combined influence of strong thermally induced repulsion from the subcooled surface and low surface wettability, the internal flow structure of the droplet undergoes significant alteration after impact. The velocity vectors become concentrated along the droplet's outer edge, exhibiting an upward deviation, while the central region shows a marked reduction in vector magnitude, indicating a tendency toward contraction.

Figure 14 compares the droplet volume index evolution after impact on surfaces with normal and low wettability at different Weber numbers. As shown in the figure, when  $We \geq 120$ , the droplet volume index on the low-wettability surface exhibits a pronounced increase. The low-wettability surface strongly constrains the droplet's motion, and lateral spreading is restricted. When the Weber number is small, and inertial impact is insufficient, the side spreading is suppressed, leading to a significantly smaller droplet volume index. However, when  $We \geq 120$ , the high-intensity inertial impact promotes the redirection of lateral momentum into vertical penetration. At this point, the concentration of vertical momentum and the transient high-pressure zone lead to a reduction in the extent of solidification, thereby leading to a significant increase in the volume index.

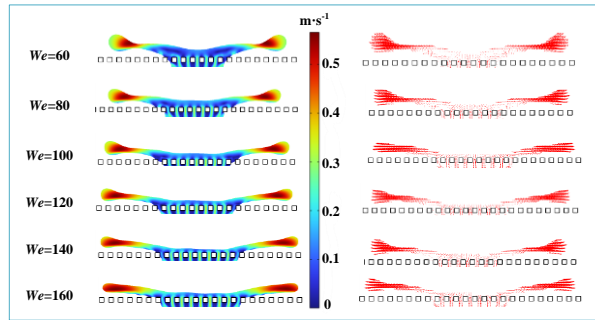


Figure 13. Spreading velocity contour and velocity vector of droplets impacting low-wettability porous structures

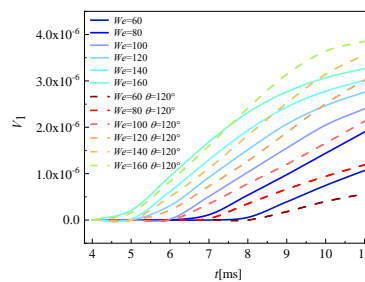


Figure 14. Variation of droplet volume index on surfaces with different wettability

### 4.3.2 Heat Transfer and Temperature Variation Characteristics of Droplet Impact on low-Wettability Subcooled Porous Structures

Figure 15 shows the temperature contour evolution of droplets impacting low-wettability porous structures, the temperature fluctuation on both sides of the droplet is more pronounced, indicating a considerable enhancement in local heat transfer intensity. The low wettability improves the adhesive connection between the droplet and the surface, inhibiting the spreading process and facilitating quick heat release at the edges, fig. 16 illustrates the temperature gradient variation. The temperature gradient distribution is mainly concentrated on the porous surface and the shallow inner walls, limiting downward heat transfer. On the low-wettability surface, although the concentrated kinetic energy leads to enhanced penetration, the extremely short contact time ensure that its total heat transfer and cumulative solidification effect remain weaker than those on the  $\theta=90^\circ$  surface. Low wettability not only regulates the droplet's motion mode but also reshapes the spatial distribution of heat transfer.

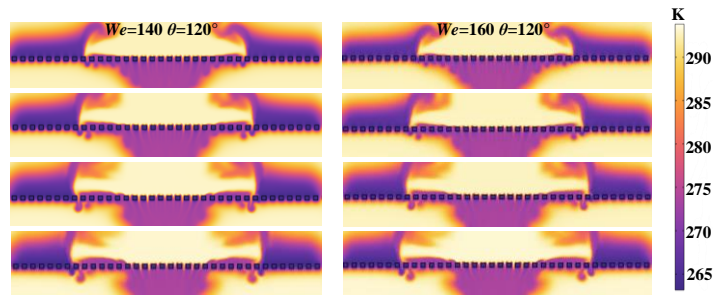


Figure 15. Temperature contour maps under low wettability

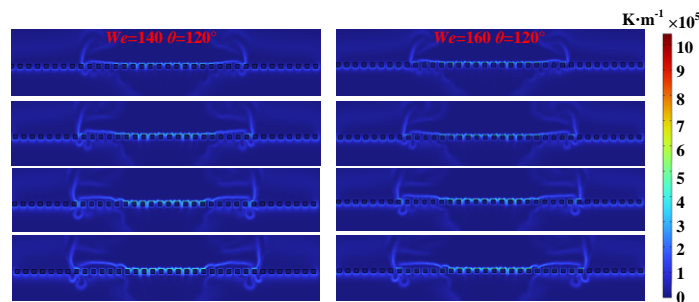
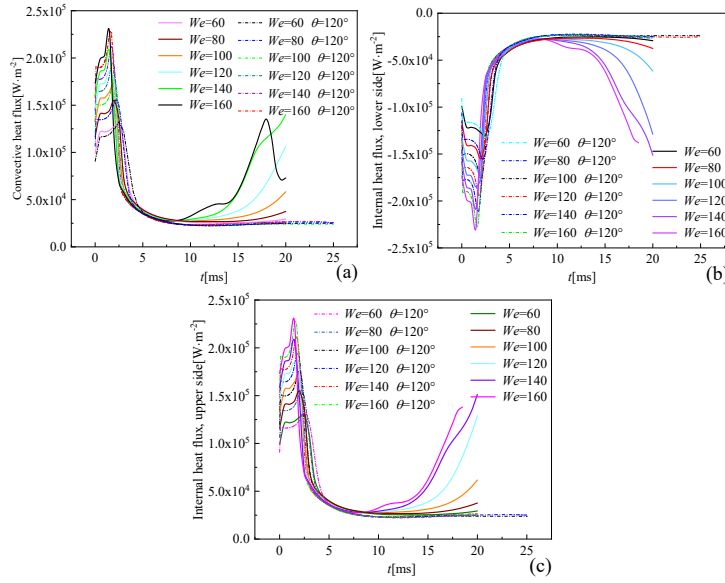


Figure 16. Temperature gradient contour maps under low wettability

As shown in fig. 17(a), (b) and (c), under high Weber number and normal wettability conditions, the heat flux exhibits a distinct double-peak profile, whereas under low wettability, the curve shows a continuously decaying trend with a substantially lower peak, indicating a reduced overall heat transfer capacity. Given the influence of low wettability on droplet spreading, penetration, and dynamic behavior, effective contact and thermal exchange between the droplet and the surface are hindered, this weakens the subsequent rebound of heat transfer, indicating that low wettability suppresses the dynamic evolution of heat transfer during droplet impact. As a result, droplets tend to completely detach from the

porous structure without undergoing repeated spreading motions on the surface. This trend reflects good ice resistance.



**Figure 17. Heat flux variations at different Weber numbers and wettability: (a) comparison of internal convective heat flux; (b) comparison of the lower side heat flux; (c) comparison of the upper side heat flux**

## Conclusion

This study systematically analyzes the heat transfer of droplet impact on porous structures. The main conclusions are summarized as follows:

(1) The porous structure significantly influences the droplet impact process. Under varying Weber numbers and surface wettability conditions, the droplet exhibits distinct differences in penetration behavior, indicating that the droplet dynamics are governed not only by its inherent kinematic properties but also by the regulating effect.

(2) Under subcooled conditions, the complexity of phase change increases. At high Weber numbers, secondary heat transfer phenomena can occur, this can be attributed to enhanced droplet fragmentation and penetration, which disrupts the continuity of the freezing process.

(3) High hydrophobicity is beneficial for the anti-icing and de-icing performance of porous structures. Although a transient increase in the volume index is observed when  $We \geq 120$ , which reflects the instantaneous influence of high inertial forces on penetration, the extremely short effective contact time and the absence of secondary heat transfer ensure that its total heat transfer and cumulative solidification effect remain weak, thereby maintaining the low overall heat transfer efficiency of the low-wettability surface.

The above research has yielded several essential insights and conclusions; however, it has several limitations, including the exclusive focus on single-droplet impacts, the inability to fully capture droplet interactions, restriction to two-dimensional simulations, simplifications in depicting actual droplet motion, and the neglect of material property variations. Consequently, future research should continue to investigate the phase change and heat transfer processes within supercooled porous structures, while systematically analyzing the effects of pore size distribution and wall material properties. Moreover, the study should be

extended to multiple-droplet impacts to better reflect realistic engineering scenarios, such as anti-icing surfaces, superhydrophobic coatings, and thermal management systems.

## Acknowledgments

This research was funded by Natural Science Basic Research Program of Shaanxi (Program No. 2025JC-YBMS-014).

## Nomenclature

Parameter	Symbol (unit)	Numerical value
Contact angle of the surface	$\theta$	90-160
Computational Domain	$\Omega$	Variable
Diameter of the droplet	$D$ [mm]	3
Dynamic viscosity of the phase-change material	$\eta$ [Pa·s]	Variable
Density	$\rho$ [kg m <sup>-3</sup> ]	1000
Dynamic Viscosity	$\mu$ [Pa·s]	Variable
Heights	$h$ [mm]	5.5
Heat Flux Density	$q$ [W·m <sup>-2</sup> ]	Variable
Initial Kinetic Energy	$E_k$ [J]	Variable
Gravitational Acceleration	$g$ [m·s <sup>-2</sup> ]	9.81
Latent Heat of Fusion	$L_f$ [kJ·kg <sup>-1</sup> ]	333
Liquid Fraction	$\beta$	Variable
Liquidus Temperature	$T_l$ [K]	Variable
Liquid Phase Volume Fraction	$\phi$	Variable
Momentum Source Term	$S_y$ [N·m <sup>-3</sup> ]	Variable
Pore size	$d$ [mm]	0.2
Porous structure temperature	$T$ [K]	263.15
Pressure	$p$ [Pa]	Variable
Spreading factor	$n$	Variable
Surface energy	$E_s$ [J]	Variable
Solidus temperature	$T_s$ [K]	Variable
Thermal conductivity	$K$ [W·m <sup>-1</sup> ·K <sup>-1</sup> ]	Variable
The initial droplet area	$A_0$ [mm <sup>2</sup> ]	7.07
The ratio of the instantaneous area	$A(t)$	Variable
the droplet volume change index	$V_1$	Variable
Velocity field	$\vec{u}$ [m·s <sup>-1</sup> ]	Variable
Weber number	$We$	60–323
Viscosity coefficient	$A_{mush}$	Variable

Volume fraction	$\varphi_l$	Variable
-----------------	-------------	----------

## References

- [1] Shen, X., et al. Study on Thermodynamic Coupling Behavior of non-Newtonian deicing fluid droplets impinging on solid wall at low temperature[J]. *Thermal Science*, (2024), 28, pp. 4089–4099.
- [2] Hongtao Zhang, et al. Cryo-powered desalination: Experimental investigations on brine droplets freezing in a natural convection environment[J]. *Desalination*, (2023), 567, 116974.
- [3] Xinyu Liu, et al. Study of seawater droplet impacting and freezing coupling processes with combined phase-field and multi-relaxation-time lattice Boltzmann method[J]. *Desalination*, (2025), 604, 118688.
- [4] Tao An, et al. Solidification process of hollow metal droplets impacting a substrate[J]. *International Communications in Heat and Mass Transfer*, (2024), 159, 108252.
- [5] Faquan Shen, et al. Numerical simulations of freezing behaviors of water droplets impacting cold hydrophobic surfaces[J]. *Applied Thermal Engineering*, (2024), 258, 124521.
- [6] Xuanchen Liu, et al. Experimental investigation on spreading and freezing mode of droplets impacting cold wall[J]. *Colloids and Surfaces A: Physicochemical and Engineering Aspects*, (2024), 703, 135375.
- [7] Anjie Hu, et al. 3D Simulations of Freezing Characteristics of Double-Droplet Impact on Cold Surfaces with Different Wettability[J]. *Entropy*, (2022), 24, 1650.
- [8] Xiaowei Yang, et al. Experimental study on freezing characteristics of droplet impact on cold cylindrical surfaces[J]. *International Communications in Heat and Mass Transfer*, (2024), 157, 107769.
- [9] Xiaobin Shen, et al. Analysis of Numerical Methods for Droplet Impingement Characteristics under Aircraft Icing Conditions[J]. *Aerospace*, (2022), 9, 416.
- [10] M. Reyssat, et al. Bouncing transitions on microtextured materials[J]. *Europhysics Letters*, (2006), 74(2), pp. 306–312.
- [11] Voller V R, Prakash C. A fixed grid numerical modeling methodology for convection diffusion mushy region phase-change problems[J]. *International Journal of Heat and Mass Transfer*, (1987), 30(8), pp. 1709–1719.
- [12] Brent A.D., et al. Enthalpy-porosity technique for modeling convection-diffusion phase change: application to the melting of a pure metal[J]. *Numerical Heat Transfer, Part A: Applications*, (1988), 13, pp. 297–318.

Submitted: 24.07.2025.

Revised: 20.12.2025.

Accepted: 22.12.2025